Advanced Energy Materials

ADVANCED ENERGY MATERIALS
www.advenergymat.de

RESEARCH ARTICLE

Multi-Domain Energy Harvesting with Mode-Dependent Magneto-Mechano-Electric Coupling

Liwei Dong[1] | Chaoyang Zhao[1] | Shuai Qu[2] | Xin Li[3] | Jiashun Li[3] | Guobiao Hu[4] | Chengjia Han[1] | Yu Zhang[5] | Ping Wang[6] | Fan Yang[7,8] | Zhong Lin Wang[9] | Yaowen Yang[1]

[1]School of Civil and Environmental Engineering, Nanyang Technological University, Singapore, Singapore | [2]College of Transportation, Tongji University, Shanghai, China | [3]Guanzhou Institute of Technology, Xidian University, Guangzhou, Guangdong, China | [4]Internet of Things Thrust, The Hong Kong University of Science and Technology (Guangzhou), Nansha, Guangzhou, Guangdong, China | [5]Department of Civil Engineering, Zhejiang University, Hangzhou, China | [6]School of Civil Engineering, Southwest Jiaotong University, Chengdu, China | [7]Department of OrthopaedicsShanghai Key Laboratory for Prevention and Treatment of Bone and Joint Diseases, Shanghai Institute of Traumatology and Orthopaedics, Ruijin Hospital, Shanghai Jiao Tong University School of Medicine, Shanghai, China | [8]Shanghai Key Laboratory of Gene Editing and Cell-based Immunotherapy For Hematological Diseases, Ruijin Hospital, Shanghai Jiao Tong University School of Medicine, Shanghai, China | [9]Beijing Institute of Nanoenergy and Nanosystems, Chinese Academy of Sciences, Beijing, China

Correspondence: Fan Yang (yfl2498@sjtu.edu.cn) | Zhong Lin Wang (wangzhonglin@binn.cas.cn) | Yaowen Yang (cywyang@ntu.edu.sg)

Received: 31 October 2025 | **Revised:** 11 January 2026 | **Accepted:** 16 January 2026

Keywords: dual-mode | magnetic field energy harvesting | synchronous electric charge extraction | vibration energy harvesting | wireless sensor node

ABSTRACT

Magnetic field energy harvesting based on the magneto-mechano-electric (MME) principle offers a promising approach for realizing self-powered Internet of Things systems. However, the magnetic fields in daily environments are stray and weak (<0.1 mT), greatly limiting the output power and practicality of conventional MME harvesters. Given the frequent coexistence of distinct-frequency magnetic field and vibration excitations in real-world scenarios, there is an urgent need for a compact and designable dual-mode harvester to unlock performance limits. Here, we present a mode-split MME harvester that leverages the first symmetric and second antisymmetric bending modes to most efficiently capture vibration and magnetic field, respectively. Mode-dependent internal couplings are integrated, where dual magnetic coupling enhances the magnetic field harvesting power density by 292%, and multi-stage internal resonance provides a 19-fold gain for vibration harvesting. The integration of the synchronous electric charge extraction technique further boosts the actual charging power by 493%, achieving a system-level charging power density of 36.59 $mW/cm^3/mT^2$. Finally, a wireless self-powered sensing system is developed and deployed in a representative trackside dual-excitation scenario. Dual-mode synergy shortens the cold start time by 56% and sensing interval by 50%. This work demonstrates a promising solution for efficient multisource energy harvesting in practical field deployments.

1 | Introduction

With the rapid growth of the Internet of Things (IoT), countless wireless sensor nodes (WSNs) have been deployed across different industrial environment to automate sensing and data collection [1], driving the advancement of Industry 4.0. As deployments scale, sustainability becomes critical, and reliance on replaceable chemical batteries must be minimized [2]. Energy harvesting technologies provide a route to self-powered operation by converting ambient energy sources such as vibration [3, 4], magnetic fields [5, 6], light [7, 8], wind [9, 10], and heat [11, 12]. In real-world environments, such as vehicle traction systems, high-speed railways, and high-voltage transmission lines, low-frequency vibrations often coexist with stray 50/60 Hz magnetic fields.

Infrastructure operating in such harsh environments requires continuous structural health monitoring. Efficiently harvesting both inputs to power sensing can reduce maintenance demands and extend service life, yet doing so requires harvesters that can operate across disparate frequencies while remaining robust to irregular excitations.

For magnetic fields at fixed frequency of 50/60 Hz, the magneto-mechano-electric (MME) harvester is an effective approach for scavenging stray magnetic energy because of their high power density [13, 14]. A typical MME harvester is a cantilever that combines a piezoelectric layer and an elastic layer with a magnetic tip mass at the free end, converting magnetic energy to electricity through mechanical motion [15–18]. Performance improvements have progressed along three complementary directions. The first direction is to optimize the energy conversion module, using low-loss piezoelectric single crystalline fibers such as PMN-PZT [19, 20], and high-performance piezoelectric ceramics such as PZT [21], PMNN-PZT [22]. In addition, Lim et al. [23] reported a triboelectric MME cantilever that delivered 708 V peak-to-peak at a magnetic field of 0.7 mT, addressing applications with high instantaneous power demand. The second concentrates magnetic flux at the harvester to form an effective field. Song et al. [24] proposed a magnetic flux concentrator for MME harvesters and achieved 3.3 mW power at a weak magnetic field of 0.8 mT, corresponding to 285% of a baseline design. Patil et al. [25] employed a magnetic lens to concentrate the weak magnetic flux, yielding a 288% enhancement over a no-lens configuration. The third optimizes the magneto-mechanical mechanisms by tailoring magnet layout, elastic-layer architecture, and mode coupling to reduce mechanical loss in conventional cantilevers. Sriramdas et al. [20] proposed a dual magnetic mass strategy that improved performance by 280% relative to a conventional cantilever. Lee et al. [26] used multilayer magnetostrictive material as the elastic layer to enhance bending moments under magnetic fields. Furthermore, mode coupling designs such as T-shaped [27], I-shaped [28], X-shaped [28], U-shaped [29], and tuning-fork structures [30] have substantially boosted output under weak fields.

Most MME harvesters maximize power by tuning their natural frequency to the magnetic field frequency. This can also enable vibration harvesting when the magnetic field and vibration excitations coincide. Dong et al. [31] first demonstrated a multi-stimuli MME harvester and showed that magnetic-field and vibration energy can be harvested simultaneously. Zhou et al. [32] explored the electrical output of a cantilevered MME harvester under combined magnetic and vibration excitation at its first three modes. However, these demonstrations assumed identical magnetic fields and vibration frequencies, a condition rarely met in practice. To improve the adaptability, Song et al. [33] introduced a multi-beam design with a bandwidth of over 30 Hz. Although the usable band is broadened, only one beam usually operates effectively at a time, which limits utilization.

In the daily living environment (Figure 1a), magnetic fields and vibrations usually coexist. Using these two sources increases the available power and enables more self-powered applications. However, vibrations near vehicle traction systems, train-induced vibration, and wind-induced galloping of high-voltage lines are typically below 50 Hz [34–37], different from the surrounding magnetic field. Moreover, the persistence and intensity of stray magnetic fields and vibrations vary substantially across scenarios, underscoring the need for a designable and efficient dual-mode energy harvesting scheme. To date, there are no reported demonstrations of simultaneously harvesting magnetic fields and vibrations at distinct frequencies. The main obstacles are: (1) flexible dual- or multi-frequency design. For cantilevered MME harvesters, it is difficult to allocate the first two modes accurately and keep them sufficiently close. (2) effective mode assignment to maximize output. Inappropriate mode selection leads to large performance imbalances, and a single structure rarely provides two modes that are each well matched to magnetic field and vibration inputs. (3) performance-enhanced strategies for random excitations. Engineering excitations, especially vibrations, are typically broadband and irregular, which depresses output, so practical systems need built-in modal coupling or other methods to boost power performance.

In our work, we introduce and demonstrate a dual-mode MME harvester capable of capturing both vibration and magnetic field energy. Our main innovation lies in proposing mode decoupling and introducing two internal coupling mechanisms, dual magnetic coupling and multi-stage resonance, to achieve designable and efficient distinct-frequency magnetic field and vibration energy harvesting. The mode decoupling realizes the first symmetric bending mode to be flexibly tuned below 50 Hz to match with vibration excitations while maintaining the second antisymmetric bending mode at 50 Hz for magnetic field harvesting. Dual magnetic coupling enhances the magnetic field harvesting power density by 292% at an extremely weak magnetic field of 0.024 mT, and multi-stage internal resonance increases the vibration harvesting power density by 19-fold at a vibration acceleration of 0.3 g ($g = 9.8\ m/s^2$). Moreover, a carefully optimized SECE interface further improves the system performance, leading to 493% enhancement in the actual extracted power. Meanwhile, an ultra-low-power WSN for wireless temperature monitoring is designed, requiring only 0.6 mJ of energy for initial startup and achieving reliable operation at only 0.02 mT. Notably, the system's performance is rigorously validated under magnetic field and irregular track vibration impacts, demonstrating reliable self-powered operation and wireless data transmission. Dual-mode synergy reduces the cold start time and sensing interval of WSN by 56% and 50%, respectively. These results provide the first practical demonstration of concurrent magnetic field and vibration energy harvesting at different frequencies, enabled by separate mode utilization and mode-dependent internal coupling.

2 | Results

2.1 | Principle of Magnetic Field/Vibration Dual-Mode Energy Harvester

An all-in-one dual-mode harvester, consisting of three host beams and two elastic support beams, is illustrated in Figure 1b. For each unit, two piezoelectric ceramics are symmetrically attached to upper surface of the host beam, and a pair of vertically symmetric magnets is placed at the beam center. This clamped–clamped design enables higher output with smaller displacement [38], enhancing the harvester's versatility and adaptability to varying magnetic field strengths across a wide range of applications. It

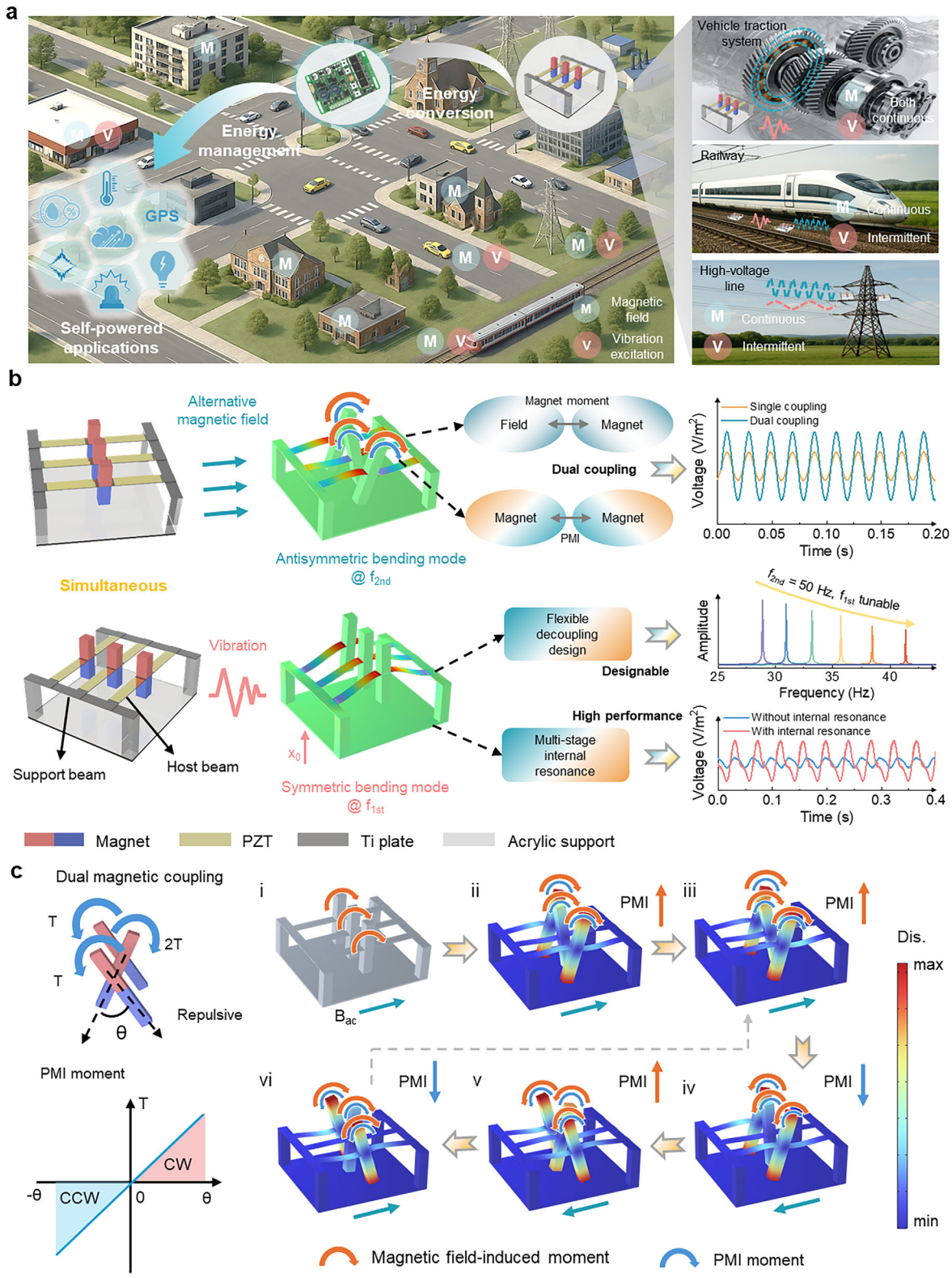

FIGURE 1 | Principle of magnetic field/vibration dual-mode energy harvester and its application scenarios. a, Application prospects of the proposed harvester in smart cities. b, Configuration and dual-mode operation of the harvester. The second antisymmetric bending mode is assigned to magnetic field harvesting, while the first symmetric bending mode is used for vibration harvesting. c, Working principle of magnetic field energy harvesting using dual magnetic coupling.

should be noted that the two ends of the host beams are not rigidly clamped and are internally coupled with other host beams through elastic support beams. Two elastic support beams link the three host beams and are fixed on an acrylic base.

In the compact structure, mode-dependent internal couplings are integrated for enhancing magnetic field and vibration energy harvesting. The structural second antisymmetric bending mode is dedicated to magnetic field harvesting. This mode matches with the excitation form of field-induced moment, enabling stronger vibrations and efficient energy coupling. In the coupled mode, the middle beam bends antisymmetrically(Figure 1b). Interactions among the permanent magnets mounted on different host beams generate additional moments that regulate the bending angle difference, aligning it with the coupled mode and thereby enhancing energy harvesting efficiency. The first symmetrical bending mode is assigned to vibration harvesting. Vertical excitation readily activates this mode, and the three-beam configuration enables multi-stage internal coupling resonance that boosts electrical output by an order of magnitude (Figure 1b). It should be noted that this mode cannot be activated under a vertical magnetic field, as the field is aligned with the magnet's polarization direction and therefore produces no magnetic field-induced moment on the magnets. A further advantage of the design is the mode decoupling design. By adjusting the elastic support beams, the first natural frequency can be shifted flexibly across the low-frequency range, while the second natural frequency remains almost unchanged. This adaptability is particularly valuable for practical engineering applications.

Specifically, the working principle of the dual magnetic coupling for magnetic field energy harvesting is illustrated in Figure 1c. When two permanent magnets are placed side by side with the same polarity, their field lines repel in the middle and bend outward, creating a lateral thrust. This lateral permanent magnet interaction (PMI) produces a moment that is nearly linear with small deflection angles, thereby amplifying beam bending and improving magnetic field harvesting efficiency. When an alternative magnetic field is just applied, field-induced moments are generated on the magnets, and they will drive the respective host beams to bend about their centers (Figure 1c-i). Owing to structural symmetry, the two outer beams bend in the same direction, whereas the middle beam bends in the opposite direction (Figure 1c-ii). This relative deflection angle generates a PMI moment, which increases the beam bending until equilibrium is reached (Figure 1c-iii). The equilibrium bending amplitude is determined by the balance between the field-induced moment and the PMI moment, and the closer this angle is to that of the coupled mode, the higher the harvesting efficiency. As the magnetic field is reversed, the bending amplitudes of all three beams decrease, and their bending direction reverses (Figure 1c-iv and v). When the magnetic field reverses again, the system transitions to the states shown in Figure 1c-vi and iii, thus realizing periodic motion and energy conversion.

2.2 | Dual Magnetic Coupling for Enhanced Magnetic Field Energy Harvesting

The introduction of PMI enables the clamped–clamped MME harvester to achieve both scalability and higher voltage/power density. In this section, we investigate how to configure PMI can allow the potential energy of permanent magnets to more effectively assist magnetic field harvesting. Figure 2a illustrates the single-beam configuration, along with its simulated magnetic flux density (mesh shown in Figure S1), time-domain voltage responses, and RMS voltages at different magnetic field intensities. When the number of beam–magnet units is expanded, the PMI effect is introduced, making magnet polarity arrangements a key factor requiring optimization.

In Configuration 2, two host beams are equipped with magnets in opposite polarity (Figure 2b). In the interaction region, their magnetic induction lines merge and attract one another, generating a mutual force along the *y*-axis (Figure 2b-i; Figure S2b). When the two host beams bend around the *y*-axis and a relative rotation angle forms between them, an attractive PMI moment is generated around the same axis (Figure 2b-ii; Figure S3a). This PMI moment enforced synchronous motion of the two magnets, resulting in voltages of piezoelectric energy harvesters (PEHs) on both host beams with nearly same amplitude and phase. (Figure 2b-iii; Figure S5). In Configuration 3, the two magnets are equipped with same polarity (Figure 2c). In the interaction region, their magnetic induction lines repel one another (Figure 2c-I; Figure S2c), producing a repulsive force along the *y*-axis whenever a relative angle develops between the two magnets (Figure 2c-ii; Figure S3b). The PMI moment promotes the rotation of one magnet while partially hindering that of the other. As a result, the voltages of PEHs on the two host beams differed, with one producing a higher output and the other a lower output. Their voltage waveforms also displayed a clear phase difference (Figure S6; Figure 2c-iii).

The two-beam configuration enables effective coordination between the two magnetic field harvesting units, resulting in a higher voltage output. To further examine the scalability of the proposed framework, three-beam structures are designed as Configurations 4 and 5 (Figure 2d,e). In Configuration 4, the middle magnet is equipped with opposite polarity to the magnets on both sides, so the magnetic field lines in the interaction region attract each other (Figure 2d-i; Figure S2d). When a relative rotation angle forms, the PMI moment acts to synchronize the motion of the three beams. However, because the torque of the middle magnet is twice that of the side magnets (Figure 2d-ii; Figure S4a), a bending angle difference is also reflected in the time-domain voltage response (Figure S7). The middle beam therefore exhibited higher voltage output compared with the sides (Figure 2d-iii). In Configuration 5, the middle magnet has the same polarity with the two side magnets, and the magnetic field lines in the interaction region repel each other (Figure 2e-i; Figure S2e). When a relative rotation angle develops, the yielded repulsive PMI moment facilitates the bending of the two side magnets, and opposite bending of the middle magnet (Figure 2e-ii; Figure S4b). As a result, there was a certain phase difference between the time-domain voltages on the middle beam and the two side beams (Figure S8). A smaller voltage was generated on the middle beam, while the side beams showed significantly enhanced voltage responses (Figure 2e-iii).

Figure 2f compares the RMS voltage outputs of the five configurations. The total RMS voltage increased with the number of host beams, confirming that the framework is scalable. Voltage

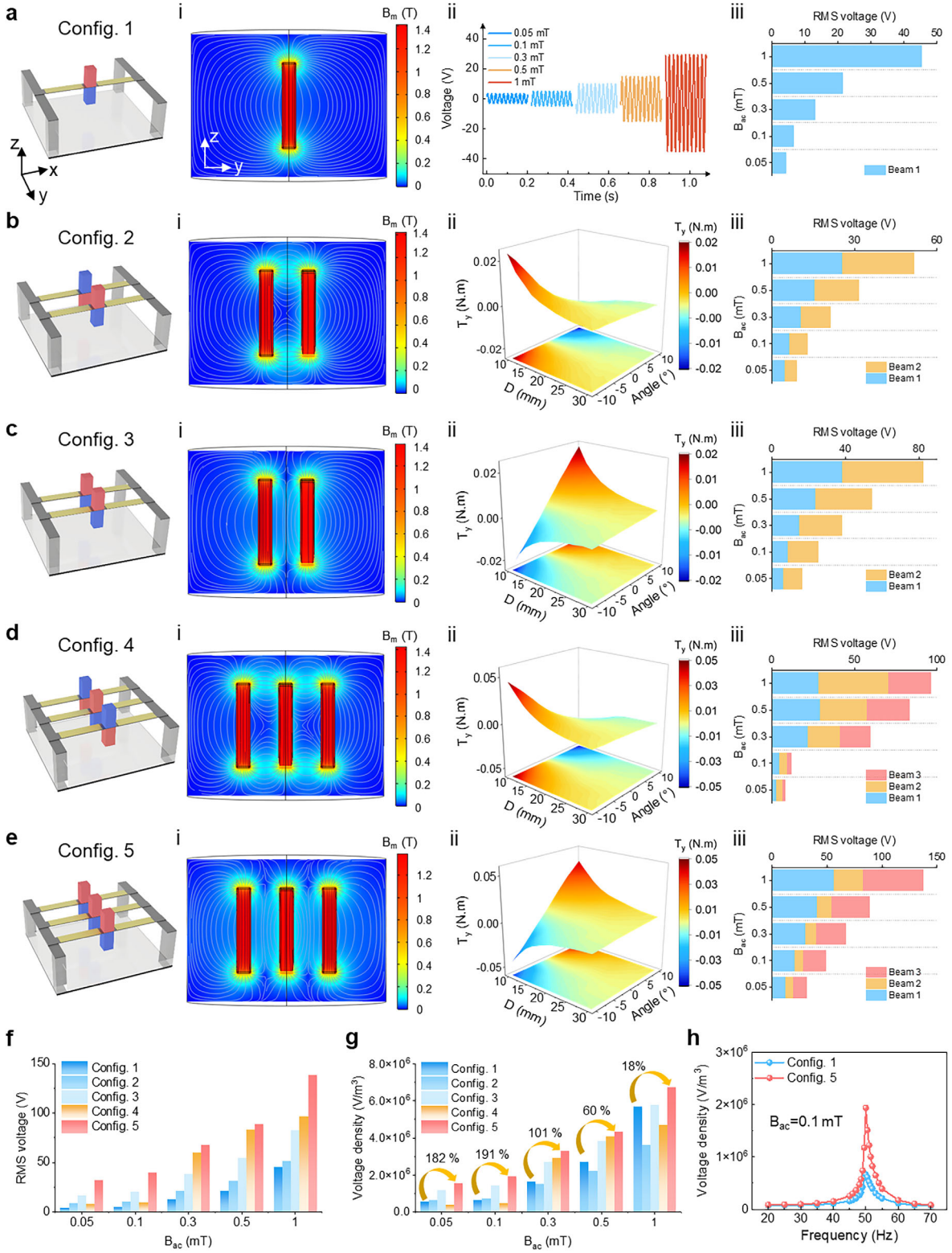

FIGURE 2 | Configurations and performance of dual magnetic coupling. a, Configuration 1 with a single-beam-magnet unit. i–iii, Simulated magnetic flux density, time-domain voltage response of one PEH, and RMS voltage of each beam at different magnetic field intensities. b, Configuration 2, consisting of two beam–magnet units with opposite polarity. i–iii, Simulated magnetic flux density, PMI moment of the right magnet, and RMS voltages at different field intensities. c, Configuration 3, consisting of two beam–magnet units with the same polarity. i, ii, iii, Simulated magnetic flux density, PMI moment of the right magnet, and RMS voltages at different field intensities. d, Configuration 4 with three beam–magnet units, where the central magnet has opposite polarity to the side magnets. i–iii, Simulated magnetic flux density, PMI moment of the middle magnet, and RMS voltages at different field intensities. e, Configuration 5, consisting of three beam–magnet units with the same polarity. i–iii, Simulated magnetic flux density, PMI moment of the middle magnet, and RMS voltages at different field intensities. f,g, Comparison of RMS voltages and voltage densities for all five configurations at different magnetic field intensities. h, Comparison of voltage density between Configurations 1 and 5 at different excitation frequencies.

densities are further evaluated using the device volume to quantify the benefits of dual magnetic coupling (Figure 2g). Configurations 3 and 5 based on repulsive PMI designs, achieved higher voltage density because the magnets' potential energy is primarily used to assist bending and to generate a bending angle difference that better matches the antisymmetric bending mode, rather than being consumed in synchronizing beam motion as in attractive designs. Among these, Configuration 5 delivered the best performance, with PMI moment increasing voltage density by up to 191% compared with Configuration 1. This advantage persisted across a wide range of excitation frequencies, maintaining high performance over a broad bandwidth (Figure 2h).

2.3 | Performance Optimization for Magnetic Field Energy Harvesting

To achieve efficient magnetic field energy harvesting, careful tuning of the host beam's second natural frequency f_{2nd} is essential. This frequency depends on both the magnet mass and the beam's geometric parameters. Beam length is inversely related to natural frequency; therefore, maintaining f_{2nd} = 50 Hz requires increasing magnet mass as the beam becomes shorter (Figure S9a). Increasing beam thickness raises its bending stiffness and requires increased magnet mass to maintain resonance, but this comes at the cost of a bulkier device (Figure S9b). Moreover, the placement of piezoelectric ceramics is also essential. To maximize conversion efficiency, they must be positioned near the central magnet, where stress is highest (Figure S9c). However, placing them too close risks collision when the magnets rotate, leading to fracture. To avoid this, a practical clearance of about 1 mm is maintained during installation.

To evaluate the harvester's performance, a test environment was setup Figure 3a, with a detailed view of the prototype provided in Figure S10. The electrical performance of Configuration 1 and Configuration 5 was further examined. Configuration 1 generated RMS open-circuit voltages and short-circuit currents of 6.76/12.3/21.6/45.4 V and 0.1/0.16/0.28/0.56 mA at B_{ac} = 0.1/0.3/0.5/1 mT, respectively (Figure S11a; Figure S11b). By contrast, Configuration 5 achieved 49.31/67.45/88.61/139.66 V and 0.675/0.88/0.95/1.6 mA under the same conditions (Figure 3c; Figure 3d). The optimal average power outputs were 0.08/0.44/1.17/5 mW for Configuration 1 at loads of 90/90/80/70 kΩ, and 2.52/5/6.83/16.55 mW for Configuration 5 at loads of 70/70/60/60 kΩ (Figure S11c; Figure 3e). Peak power performance of the two configurations is provided in Figure S12. Under a fixed load of 70 kΩ, Configuration 5 exhibited up to 20-fold higher average power and 7-fold higher average power density compared with Configuration 1. (Figure S13). This improvement decreased with rising B_{ac}, as the field-induced moment gradually dominates over PMI at higher field strengths.

Configuration 5 is selected as the final design because of its outstanding performance. In this configuration, the repulsive moment generated by the three magnets with identical polarity promotes clockwise motion in beam 1/3 and counterclockwise motion of beam 2, enabling better alignment with the structural coupling mode (Figure 1b) and thereby achieving optimal performance (more detailed explanation provided in Figure S14 and Note S1). Figure 2e-ii show that reducing the magnet distance D significantly enhances the PMI moment. Therefore, Figure 3f,g examine the effects of different D values on the harvester performance. It is evident that under magnetic fields greater than 0.1 mT, a smaller D effectively enhances the energy harvesting performance. However, the performance under weak magnetic fields below 0.1 mT is of greater concern in the field of magnetic field energy harvesting [28, 29, 38], as it more closely reflects the conditions encountered in most practical application scenarios. As shown Figure 3g, at a relatively large distance of D = 20 mm, the harvester achieved its best performance under an ultralow magnetic field of 0.02 mT. However, as the magnetic field increases, its performance advantage diminished, owing to the decreasing proportion of the PMI moment relative to the field-induced moment. When the distance D was reduced to 12 mm, the PMI moment increased, and the performance advantage for B_{ac} > 0.06 mT became evident.

To highlight the advantages of dual magnetic coupling under weak magnetic fields, we compared our proposed design with our single clamped–clamped MME harvester and with the one reported in [38] (Figure 3h). When B_{ac} < 0.05 mT, the harvester with a D of 20 mm achieved optimal performance. Especially, at B_{ac} = 0.024 mT, the average power density of the multi-beam design was 3.13 and 3.92 times those of the single clamped-clamped MME harvester in our work and [38], respectively. The harvester with a D of 12 mm achieved best performance when B_{ac} > 0.05 mT; but at B_{ac} = 0.024 mT, its performance even fell below that of a single clamped–clamped MME harvester. A noteworthy trend is that the normalized average power density decreases as the magnetic field increases, indicating reduced energy harvesting efficiency per unit magnetic field at higher field intensities. This is mainly attributed to the one-sided amplification of the magnetic field-induced moment, which reduces the proportion of the PMI moment in the total moment and ultimately degrades the system performance. Our simulations support this trend (Figure S16 and Note S2). Meanwhile, under weak magnetic fields of 0.024 mT and 0.048 mT, reducing the magnet spacing D may reduce the performance, mainly due to the pre-twist of the beams caused by asymmetric lateral forces between the magnets, which hinders their motion. In practical implementation, small deviations in magnet properties, alignment, and beam parameters are difficult to avoid and potentially amplify this pre-twist effect. More detailed explanations are provided in Figures S15–S18 and Note S2. Because our focus is on the harvester's performance under extremely weak magnetic fields, D = 20 mm is selected as the final parameter. A design map for a multi-beam harvester is also provided in Figure S19 and Note S3.

To further boost the harvester's performance under extremely weak magnetic fields, the SECE technique is integrated in the proposed system (Figure S20). In this approach, the piezoelectric charge is extracted at the voltage peak and transferred through an inductor to a storage capacitor via a controlled switch, enabling synchronous charge release and high mechanical–electrical conversion efficiency (Figure 3i). The charge extraction inductor is carefully optimized for our harvester, increasing the capacitor voltage by 143%, leading to a 493% enhancement in the actual extracted power (Figure 3j). As a result, a 10,000 μF capacitor was charged to 3 V with only 40 s at 0.1 mT (Figure 3k). With the proposed configuration, the harvester can

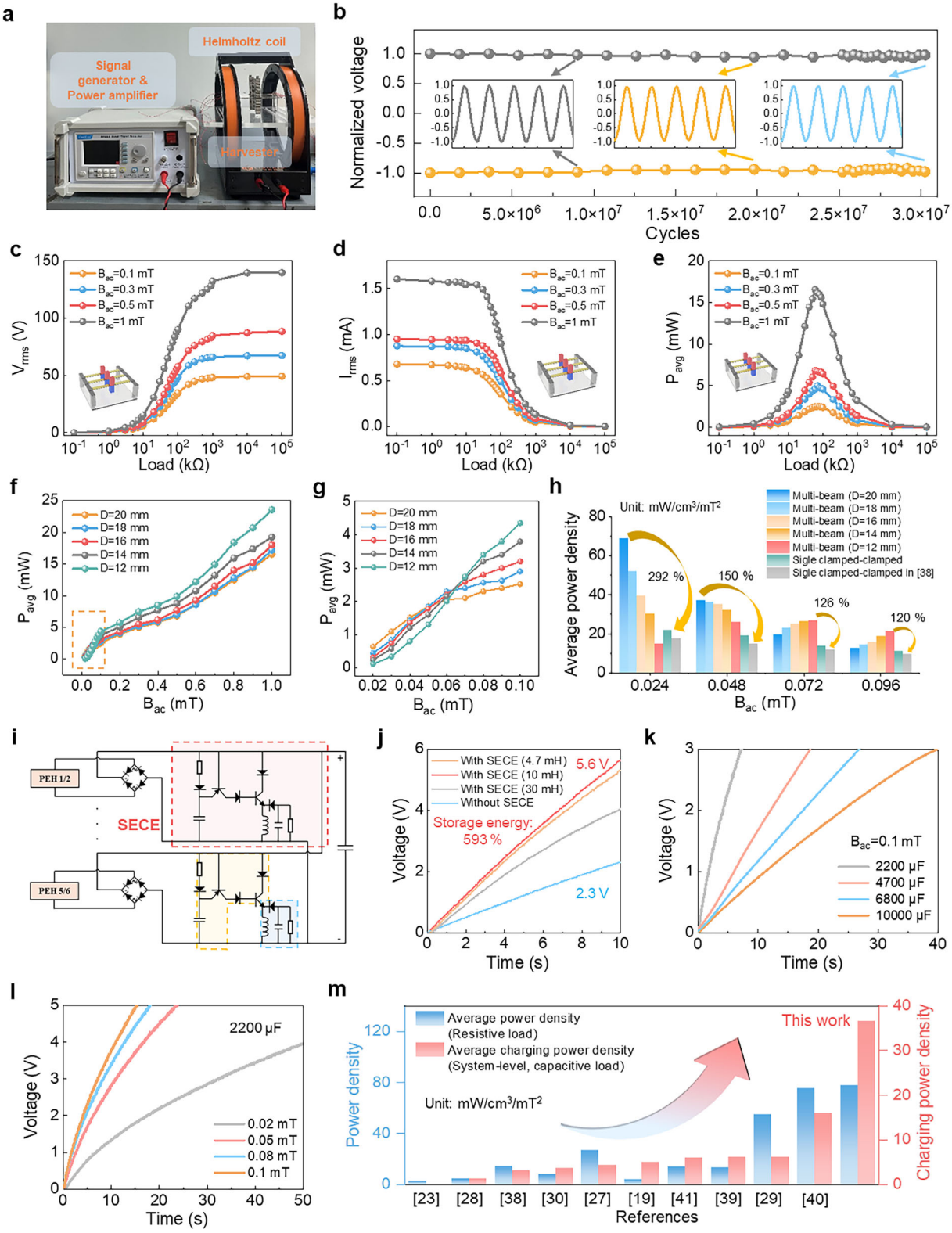

FIGURE 3 | Performance optimization for magnetic field energy harvesting. a, Experimental setup for magnetic field energy harvesting evaluation. b, Durability validation with over 30,000,000 cycles at B_{ac} = 0.1 mT. c–e, RMS voltage, RMS current, and average power of Configuration 5 under the same conditions. f, g, Average power of harvester at different magnet distance D, and a detailed view below 0.1 mT. h, Comparison of power density between the proposed multi-beam design and a single clamped-clamped MME harvester. i, Circuit configuration with SECE technique for capacitor charging tests. j, Optimization of energy extraction inductor and comparison of the voltage charging curves of a 2200 μF capacitor with and without the SECE technique. k, Time-domain voltage curve of capacitors with different capacitance at B_{ac}=0.1 mT. l, Time-domain voltage curve of a 2200 μF capacitor at $B_{ac} \leq 0.1$ mT. m, Comparison of the proposed harvester with other recently reported MME harvesters.

charge a 2200 μF capacitor under an extremely low magnetic field of 0.02 mT, achieving an average charging power density of 36.59 mW/cm^3/mT^2 (Figure 3l), which is 10 times higher than the 3.2 mW/cm^3/mT^2 obtained by a single clamped–clamped MME harvester in [38].

The durability of harvesters is critical, as it determines their reliability in engineering applications. After 30,000,000 cycles under a 0.1 mT magnetic field, both the multi-beam design and the single clamped–clamped design maintained stable output without significant degradation (Figure 3b; Figure S21), which is consistent with the durability of single clamped–clamped one reported in [38] under the same magnetic field condition. In addition, the performance of the harvesters under environmental variations is investigated. When the temperature increases from 20°C to 70°C, the voltage output showed a decreasing trend, with the multibeam design dropping by 18% and the single clamped–clamped MME harvester dropping by 13% (Figure S22a). The larger decline in the multi-beam design is attributed partly to the temperature-induced degradation of piezoelectric material performance, and partly to temperature-related shifts in the natural frequency, which have a more pronounced effect on the resonance behavior of multi-beam systems. Both harvesters exhibited no significant change within the relative humidity range of 30–80% (Figure S22b).

As shown in Figure 3m, the normalized average power density of the harvester and the normalized system-level average charging power density are compared with the recently reported MME systems. The normalized power density is obtained by dividing the average power by the device volume and normalizing the magnetic field strength to evaluate the harvester's ideal power performance, while the latter is derived by using the actual charging power of the complete energy harvesting system for capacitive loads, thereby providing a more representative measure of the system's performance in practical applications. Our system achieves a normalized power density of 78.04 mW/cm^3/mT^2 and a system-level charging power density of 36.59 mW/cm^3/mT^2, representing superior performance among recently reported works, owing to the dual magnetic coupling design and the optimized SECE circuit. Detailed data for the calculations are provided in Table S2 [19, 23, 27–30, 38–41].

2.4 | Multi-Stage Internal Resonance for Enhanced Vibration Energy Harvesting

In our proposed framework, simultaneous magnetic field and vibration energy harvesting are expected, with a flexible and robust mode decoupling design. To achieve efficient magnetic field harvesting, f_{2nd} must be tuned to 50 Hz by appropriately designing host beam parameters (Figure 4a). This adjustment also influences f_{1st}, so the host beam parameters should be chosen carefully to keep f_{1st} close to the vibration excitation frequency (Figure S23). Importantly, f_{1st} can then be further tuned by modifying the support beam parameters or adjusting the spacing between the magnets, which hardly affects f_{2nd}, thus realizing design decoupling for vibration and magnetic field harvesting.

It is worth noting that in the vibration harvesting mode, multi-stage internal resonance among the host beams is achieved to boost electrical output. As the lumped-parameter model shown in Figure 4b, each piezoelectric beam is represented as an equivalent mass–spring–damping unit. Owing to the structural symmetry, the two support beams can be assumed to move identically and are therefore also simplified as a single mass–spring–damping unit. Integrating these components, the governing equation of the coupled system can be expressed as

$$\begin{cases} M_1\ddot{x}_1 + C_{hb}(\dot{x}_1 - \dot{x}_{sb}) + K_{hb}(x_1 - x_{sb}) + 2\theta V_1 = 0 \\ C_P\dot{V}_1 + I_1 - \theta(\dot{x}_1 - \dot{x}_{sb}) = 0 \end{cases} \quad (1)$$

$$\begin{cases} M_2\ddot{x}_2 + C_{hb}(\dot{x}_2 - \dot{x}_{sb}) + K_{hb}(x_2 - x_{sb}) + 2\theta V_2 = 0 \\ C_P\dot{V}_2 + I_2 - \theta(\dot{x}_2 - \dot{x}_{sb}) = 0 \end{cases} \quad (2)$$

$$\begin{cases} M_3\ddot{x}_3 + C_{hb}(\dot{x}_3 - \dot{x}_{sb}) + K_{hb}(x_3 - x_{sb}) + 2\theta V_3 = 0 \\ C_P\dot{V}_3 + I_3 - \theta(\dot{x}_3 - \dot{x}_{sb}) = 0 \end{cases} \quad (3)$$

$$M_{sb}\ddot{x}_{sb} + C_{sb}(\dot{x}_{sb} - \dot{x}_0) + K_{sb}(x_{sb} - x_0) - C_{hb}(\dot{x}_1 - \dot{x}_{sb}) - K_{hb}(x_1 - x_{sb}) - C_{hb}(\dot{x}_2 - \dot{x}_{sb}) - K_{hb}(x_2 - x_{sb}) - C_{hb3}(\dot{x}_3 - \dot{x}_{sb}) - K_{hb3}(x_3 - x_{sb}) = 0 \quad (4)$$

where M_n (n = 1, 2, 3), C_{hb}, and K_{hb} represent the equivalent mass, damping, and stiffness of the host beams, respectively. θ, C_p, V_n, and I_n (n = 1, 2, 3) denote the electromechanical coupling coefficient, equivalent capacitance, voltage, and current of the PEHs, respectively. M_{sb}, C_{sb}, and K_{sb} refer to the equivalent mass, damping, and stiffness of the support beam, respectively.

Finite element simulations were performed to visualize the coupled modes of the system (Figure 4c). Coupled mode 1 corresponds to the first symmetrical bending mode of the host beams and operates with internal resonance among the three beams. It is the primary mode for vibration energy harvesting at f_{1st}. Coupled mode 2 provides additional vibration harvesting capacity at $f_{1st\text{-}b}$. Coupled mode 3 is associated with the second antisymmetric bending mode of the host beams for magnetic field energy harvesting at f_{2nd}. In the decoupling design of f_{1st} and f_{2nd}, increasing support beam length reduces its equivalent stiffness, thereby lowering f_{1st}, while f_{2nd} remains nearly constant (Figure 4d). This adjustment also enhances direct vibration coupling and the internal resonance among the host beams, resulting in higher voltage output. Similarly, reducing the spacing between host beams D decreases f_{1st} and promotes inter-beam interactions (Figure 4e). Support beam thickness is another parameter for tunning f_{1st} (Figure S24), however, it is difficult to adjust once selected, requiring careful design at the beginning.

Vibration energy harvesting test environment was established to evaluate the harvester's performance (Figure 4f; Figure S25). Figure 4g shows the time-domain responses of the PEHs on the three host beams at f_{1st}, with voltage amplitudes and phases nearly identical. It arises from the symmetrical lateral repulsion between the upper and lower permanent magnets. The three peaks in voltage and power corresponded directly to the three coupled modes, broadening the bandwidth. At f_{1st} of 24 Hz, the harvester achieved a maximum RMS voltage of 46 V, an average power of 1.88, and a peak power of 8.76 mW (Figure 4h,i). Owing to internal resonance, power generation performance was

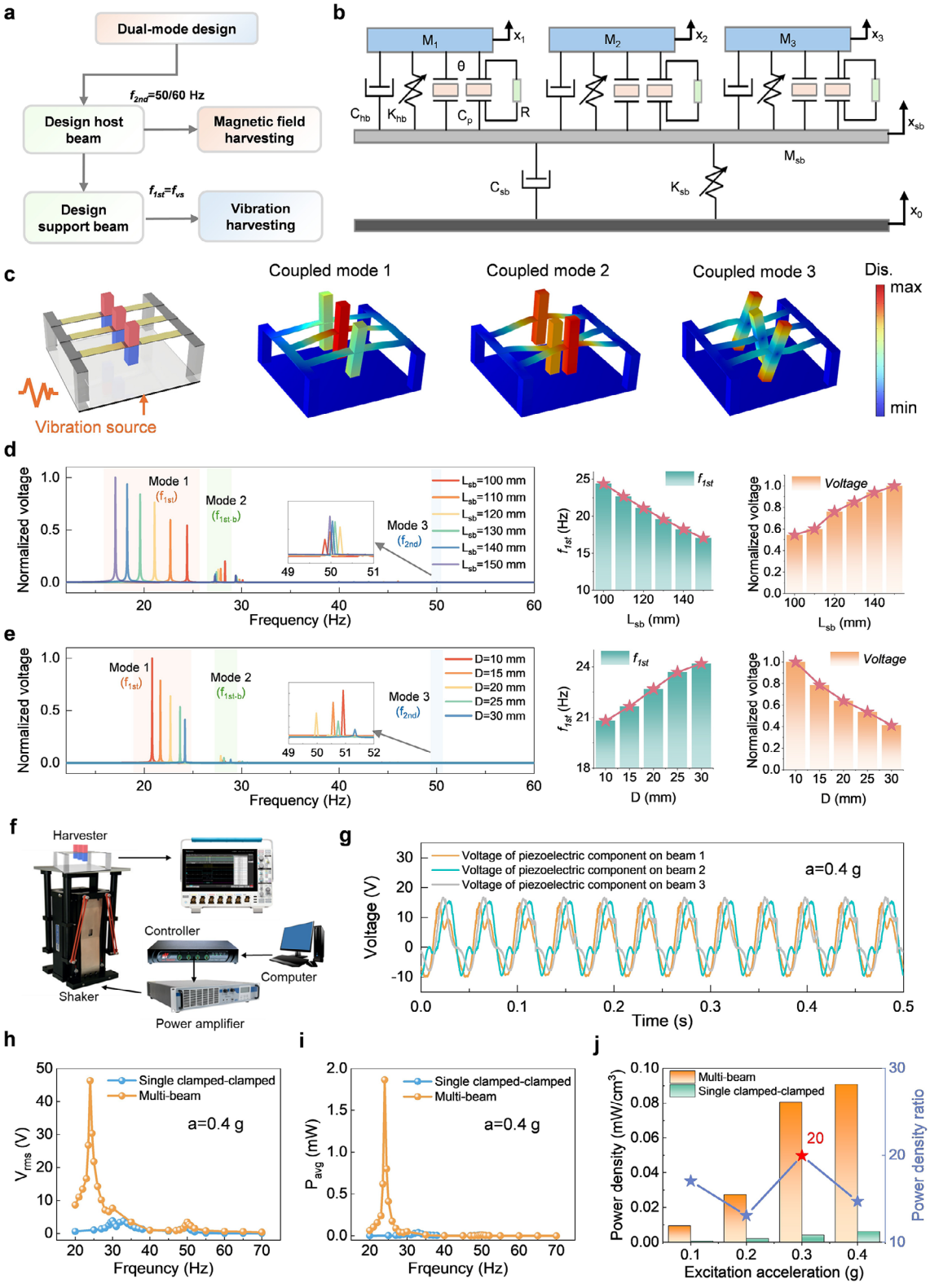

FIGURE 4 | Multi-stage internal resonance design for vibration energy harvesting. a, Mode-split design for simultaneous magnetic field and vibration energy harvesting. b, Lumped-parameter dynamical model of the proposed harvester. c, Three main coupled modes of the multi-beam structure. d, Effect of support beam length on frequency response, first natural frequency, and voltage output. e, Effect of spacing between host beams on frequency response, first natural frequency, and voltage output. f, Experimental setup for vibration energy harvesting performance evaluation. g, Time-domain voltage response of the harvester under 0.4 g excitation. h,i, RMS voltage, and average power of single-beam and multi-beam configurations at different excitation frequencies under a constant acceleration of 0.4 g. j, Average power density and power density enhancement of the multi-beam configuration at different excitation accelerations.

amplified by an order of magnitude, with the average power increasing by up to 64-fold and the power density by 19-fold under 0.3 g excitation (Figure S28; Figure 4j). Time-domain voltage responses of multi-beam and single-beam configurations at different vibration accelerations are provided in Figures S26 and S27. These findings demonstrate that multi-stage internal resonance yields giant improvements in vibration energy harvesting performance, enabling practical applications even under weak vibrations.

2.5 | Application Demonstrations

We demonstrated the harvester's practicality through several self-powered applications. It successfully lighted 400 LEDs at 0.1 mT (Figure 5b; Movie S1), and powered six bulbs, each with a rated power of 1 W, at 0.3 mT using a configuration with a magnet distance of 12 mm (Figure 5c; Movie S2).

Additionally, the harvester was used to power two commercial hygrometers connected in parallel at B_{ac} = 0.1 mT (Figure 5d). At the beginning, the capacitor was charged and the operational voltage increased gradually (Figure 5e). The hygrometers then operated in an undervoltage state at around 1 V, with dim display brightness. Once the voltage reached approximately 1.2 V, the hygrometers functioned normally. Its operational voltage continued to rise, indicating surplus energy. When the magnetic field was cancelled, the voltage quickly dropped below 1.0 V, and the hygrometers shut down.

We further developed a wireless self-powered temperature monitoring system to demonstrate its IoT applications (Figure 5a). The integrated WSN, consisting of SECE units and rectifier units (RU), an energy management unit (EMU), and a signal transmission unit (STU), integrates functions of energy enhancement and management, temperature sensing, and signal transmission (Figure 5f; Figure S29). The RU converts the AC voltage into DC voltage using six full-bridge rectifiers. The EMU then stabilizes the output with a capacitor and regulates power delivery through a buck converter. This converter incorporates an undervoltage lockout (UVLO) mechanism to prevent inefficient operation at low voltages and features an energy-indication design for robust performance under variable conditions. Finally, the STU is powered by the stabilized DC voltage, enabling temperature sensing and wireless data transmission. The WSN features an ultra-low-power design with an initial startup energy of only 0.6 mJ, which is one order of magnitude lower than that of other WSNs designed for MME harvesters (Table S3). Powered by the proposed energy harvesting system, it can be successfully started under a magnetic field as low as 0.02 mT.

The voltage of the WSN was monitored to evaluate its operational status when powered by the harvester with a magnet distance of 20 mm. At a weak B_{ac} of 0.05 mT, the system operated intermittently, transmitting temperature data each time the WSN voltage reached 5 V (Figure 5g). When B_{ac} was increased to exceed 0.1 mT, continuous operation was achieved after the voltage reached 5 V for the first time. The input energy was surplus to allow the voltage to finally stabilize at approximately 20 V (Figure 5h; Figure S30). Under stronger magnetic fields, the cold start time shortened significantly from 4.74 to 0.3 s, and continuous temperature sampling at 1 Hz was achieved when $B_{ac} \geq 0.1$ mT (Figure S31).

2.6 | Trackside Applications Under Dual Excitations

As shown in Figure 4d and Figure S32, the multi-beam MME harvester features a mode decoupling design, supporting independently designable magnetic field and vibration energy harvesting at distinct frequencies. For conventional cantilever and single clamped–clamped MME harvesters, variation of any single structural parameter inevitably affects both the first and second dominant frequencies simultaneously. As a result, multi-parameter optimization is required to achieve the desired dual-frequency design; however, optimization in a high-dimensional parameter space is extremely time-consuming and challenging. Another limitation of the single clamped–clamped MME harvester is its weak vibration energy capture capability in the first vibration mode (Figure 4i,j). In contrast, in our multi-beam design, this capability can be significantly enhanced through internal resonance among multiple beams.

To validate the harvester's ability to simultaneously capture magnetic field and vibration excitations, we installed it on a sleeper in a real-world railway system for rail temperature monitoring (Figure 6a). Temperature monitoring is essential for seamless steel rails. When rail temperature rises more than 20°C above the locking temperature, an alarm must be triggered, and maintenance should be carried out immediately to ensure operational safety. In our concept, as a train passes the monitoring point, both train-induced vibration and magnetic field excitations power the WSN, enabling wireless transmission of rail temperature data to the train, and reducing the need for frequent manual inspection.

To achieve this goal, we first evaluated train-induced sleeper vibrations using a vehicle-track coupled dynamics model (Figure 6b-i Figure S33). The vehicle model adopted the CRH350 train model operating at 300 km/h, and the track model employed 60 kg/m rails. The RMS acceleration of the wheel–rail impact was approximately 1.6 g, with multiple low-frequency peaks below 50 Hz and the dominant component centered at 30 Hz (Figure S34). To match these conditions, the tightness of our rail fasteners was adjusted so that the dominant frequencies transmitted to the sleepers aligned with the predicted first two frequencies of 25 and 30 Hz (Figure 6b-ii). Following the design process shown in Figure 4a, the harvester was reconfigured so that its first three coupled modes (Figure 4c) were located at 25, 30, and 50 Hz, respectively (Figure 6b-iii), with the first two for random sleeper vibration and the third for magnetic field harvesting. Finally, the reconfigured harvester was installed in a prepared railway track system. Train-induced vibrations were simulated using a force hammer, and traction current across the rail was emulated with an alternative magnetic field (Figure 6b-iv). The magnetic field around steel rails is typically less than 2 mT [44]; here, a weaker magnetic field of 0.02 mT was applied to validate the harvester's operation under extreme conditions. The vibration excitation was controlled at an RMS value of 1.6 g, consistent with the predicted results.

As shown in Figure 6c,d, the harvester operated effectively under single excitations, with the dominant frequencies of the output

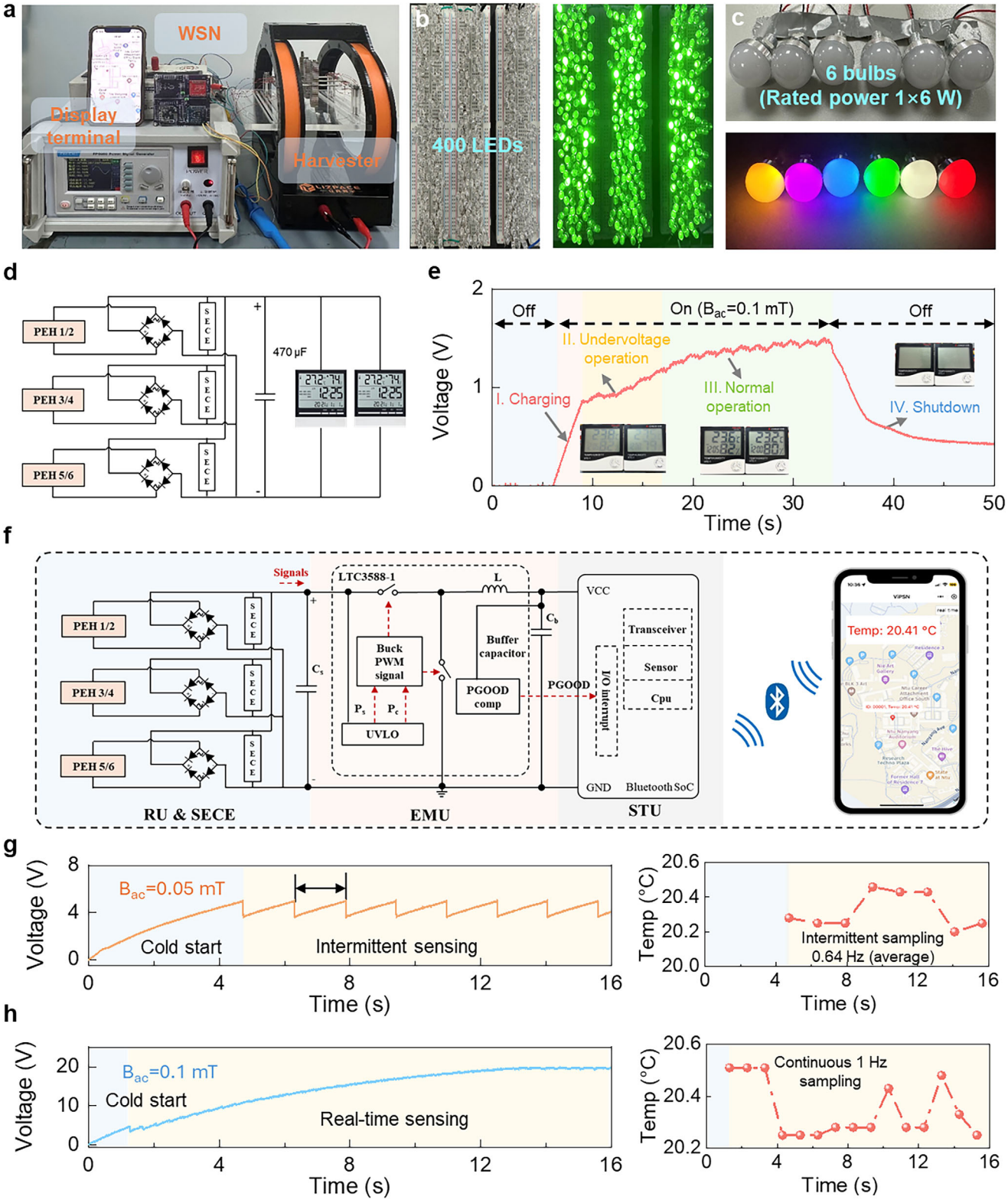

FIGURE 5 | Self-powered application demonstrations. a, Photograph of the harvester powering a WSN for mobile temperature monitoring. b, Demonstration of the harvester lighting 400 LEDs at 0.1 mT. c, Demonstration of the harvester powering six bulbs, each with a rated power of 1 W, at 0.3 mT. d, Circuit configuration for powering two commercial hygrometers in parallel. e, Time-domain operational voltage of the two hygrometers powered by the harvester at B_{ac}=0.1 mT. f, Circuit configuration of a customized low-power WSN for mobile temperature monitoring. g,h, Time-domain operational voltage of the WSN and corresponding temperature signals when powered by the harvester at B_{ac}=0.05 and 0.1 mT.

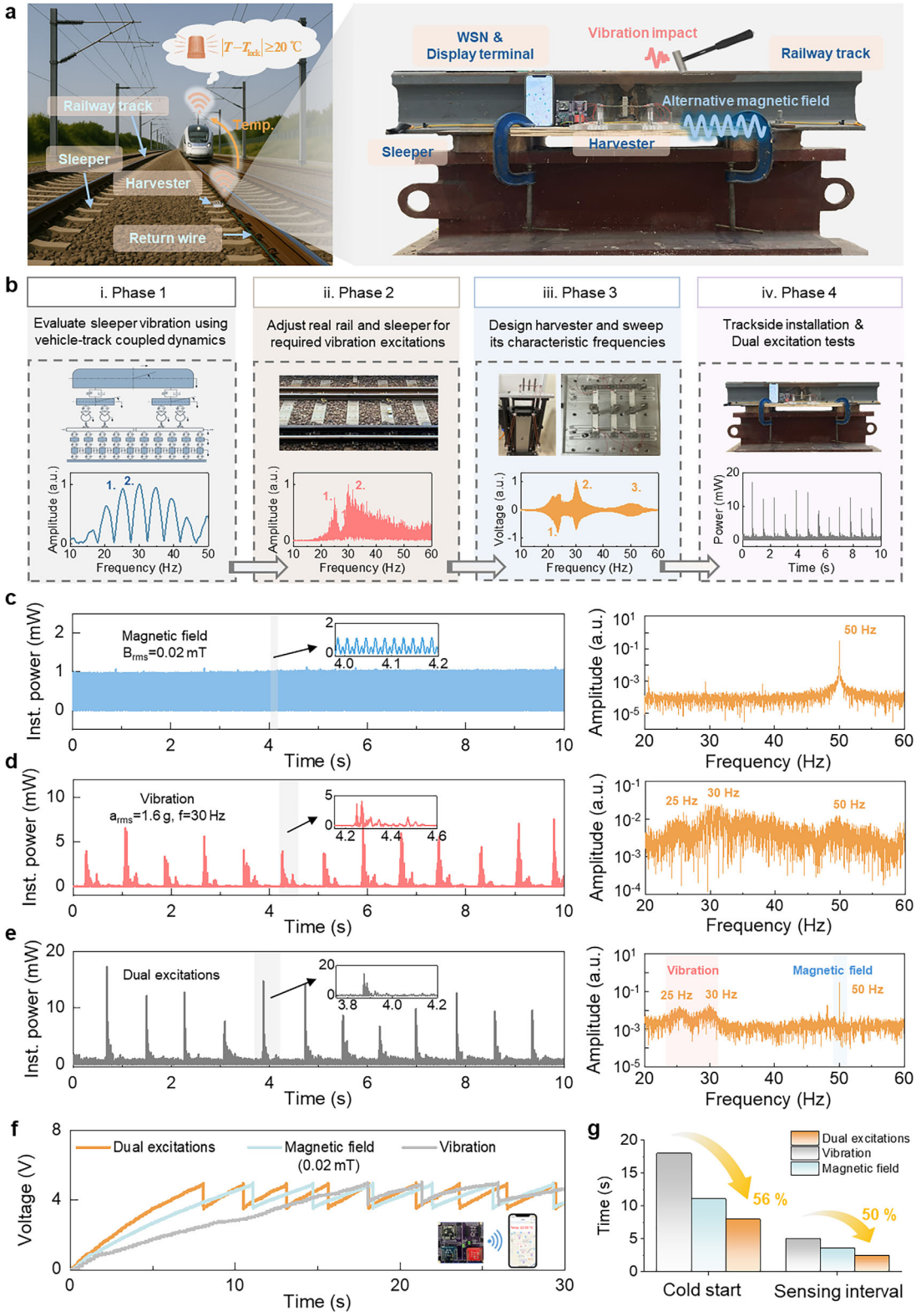

FIGURE 6 | Trackside application and dual-excitation tests. a, Schematic of the harvester deployed for high-speed railway rail temperature monitoring and warning, and a photograph of the harvester installed in a real railway track system. b, Design process of the harvester tailored to dual excitations near railway tracks. c, Instantaneous power output of the harvester under magnetic-field excitation (B_{rms} = 0.02 mT) and its corresponding frequency-domain characteristic. d, Instantaneous power output of the harvester under vibration excitation (a_{rms} = 1.6 g and f = 30 Hz) and its corresponding frequency-domain characteristic. e, Instantaneous power output of the harvester under dual excitations and its corresponding frequency-domain characteristic. f, Time-domain operational voltage of the WSN powered by the harvester under magnetic field, vibration, and dual excitations. g, Comparison of cold start time and sensing internal of the WSN under magnetic field, vibration, and dual excitations.

power matching the corresponding natural frequencies. When magnetic field and vibration excitations were applied simultaneously, their time-domain features were superimposed, and the output power exceeds that obtained under either excitation alone. In the frequency domain, distinct peaks appeared at 25, 30, and 50 Hz, confirming simultaneous harvesting of vibration and magnetic field energy (Figure 6e). Furthermore, powering the WSN in dual-excitation mode reduced the cold start time and sensing interval by 56% and 50%, respectively (Figure 6f,g). These results highlight the capability of the dual-mode harvester to exploit multiple energy sources simultaneously, significantly improving power generation efficiency.

3 | Conclusion

This work developed and prototyped a mode-split MME harvester that employs mode-dependent internal couplings to simultaneously capture stray magnetic fields (50/60 Hz) and low-frequency mechanical vibrations. By assigning magnetic and vibration excitations to their most compatible bending modes, the harvester achieves efficient dual-mode energy harvesting. Experimental results showed a system-level charging power density of 36.59 $mW/cm^3/mT^2$ at 0.02 mT for magnetic field energy harvesting, substantially outperforming previously reported MME energy harvesting systems. The introduction of dual magnetic coupling yields a 292% increase in power density for magnetic field energy harvesting at 0.024 mT, while multi-stage internal resonance enhances the vibration harvesting power density by 19-fold at 0.3 g, compared with the single clamped–clamped MME harvester. These findings demonstrate the effectiveness of mode-dependent couplings in achieving high energy harvesting efficiency under weak excitations.

Beyond device-level characterization, a self-powered railway sensing system was developed for wireless rail temperature monitoring. In the system, an energy management circuit comprising the SECE unit, LTC3588-1 management module, and signal acquisition and transmission module was integrated, where the SECE boosts the actual extracted power by 493%. For real railway track applications, the harvester was reconfigured so that its first two coupled modes aligned at 25 and 30 Hz for train-induced sleeper vibrations, and the third at 50 Hz for the alternative magnetic field generated by rail return current. Under dual excitations, both the time-domain output and frequency response confirmed genuine co-harvesting rather than source switching. The combined input reduced the cold start time and sensing interval of the WSN by 56% and 50%, respectively, demonstrating cooperative enhancement of energy availability.

To the best of our knowledge, this is the first practical demonstration of simultaneous magnetic fields and vibration harvesting at distinct frequencies. Compared with conventional MME harvesters, the proposed mode-split design achieves higher electrical output, tunable frequency configuration, and genuine dual-mode operation, making it particularly suitable for powering distributed sensors in environments with coexisting magnetic and vibration sources. Overall, this work advances the environmental adaptability and engineering practicality of dual-excitation MME harvesters, offering a promising pathway toward energy self-sufficient IoT systems.

4 | Experimental Section

4.1 | Simulations of Dual-Mode Harvester

The moment generated by permanent magnet interaction was simulated using COMSOL Multiphysics 5.6 via the magnetic field module. During harvester design, solid mechanics, electrostatics, and circuit modules were coupled to calculate modal shapes, natural frequencies, and electrical responses. Sleeper vibrations were evaluated using a vehicle-track coupled dynamics model programmed in MATLAB R2019a and solved with the Zhai method [45], with a time step size of 1×10^{-4} s. A detailed calculation process and the parameters used are provided in Note S4 and Table S4.

4.2 | Fabrication of Dual-Mode Harvester

The harvester consists of three host beams, two support beams, permanent magnets, four support columns, and a base. The host beams were fabricated from Ti plates with a width of 10 mm and a thickness of 0.4 mm, while the support beams used plates of the same width and a thickness of 0.8 mm. PZT-5H ceramics were symmetrically bonded to upper surface of the host beams using epoxy resin adhesive and cured for 24 h. N52 NdFeB permanent magnets were mounted at the center of each host beam and vertically arranged in a symmetric configuration. The three host beams were connected to the two supporting beams with epoxy resin adhesive and cured for 24 h. Four acrylic support columns were used to connect the support beams to an acrylic base, secured by screws.

4.3 | Electrical Measurement of Dual-Mode Harvester

For magnetic field energy harvesting tests, an AC magnetic field generator was used, providing a frequency range of 0–50 kHz and a maximum field intensity of 1.8 mT at 50 Hz. Vibration energy harvesting tests were carried out using a vibration shaker (APS 113). Electrical signals from the dual-mode harvester were acquired with a four-channel oscilloscope (Tektronix MSO44). For resistance optimization and capacitor charging tests, a resistance decade box (IET RS-200 W) and a capacitance decade box (IET RCS-500) were employed.

4.4 | Hardware Implementation of the WSN Circuit

The circuit board of the energy-indication WSN was designed and implemented using Altium Designer 20. The EMU was based on a buck-converter controller chip (LTC3588-1), which regulates voltage with an energy-conversion efficiency of 80–90%. A low-power voltage comparator (MIC841) with adjustable hysteresis was integrated to control the circuit's operating modes. The STU was designed around a Bluetooth system-on-chip nRF52832.

4.5 | Real Railway Track Installation and Demonstration

A real railway track system was used to replicate actual application scenarios of the harvester. The tightness of the fasteners

was adjusted so that the vibration frequency characteristics of the sleeper matched the predicted train-induced vibrations. The harvester was rigidly mounted on the sleeper using screws. Both magnetic field and vibration excitations were applied simultaneously to verify dual-stimuli performance and improvement in powering the WSN. During the test, the operational voltage of WSN was measured with a data acquisition module (NI 9229) and recorded using SignalExpress software on a computer.

Acknowledgements

This research is sponsored by the NTU grant 020671-00001, the National Natural Science Foundation of China (Grant Number. 12202276), Fundamental Research Funds for the Central Universities (Grant Number. YG2025ZD18), Shanghai Municipal Health Commission (Grant Number. 2024ZZ2002), Guangdong Basic and Applied Basic Research Foundation under Grant Number.2025A1515011342, and Innovative research team of high-level local universities in Shanghai.

Conflicts of Interest

The authors declare no conflicts of interest.

Data Availability Statement

The data that support the findings of this study are available from the corresponding author upon reasonable request.

References

1. L. Portilla, K. Loganathan, H. Faber, et al., "Wirelessly powered large-area electronics for the Internet of Things," *Nature Electronics* 6 (2023): 10–17.

2. Z. L. Wang and W. Wu, "Nanotechnology-Enabled Energy Harvesting for Self-Powered Micro-/Nanosystems," *Angewandte Chemie International Edition* 51 (2012): 11700, https://doi.org/10.1002/anie.201201656.

3. L. Dong, Y. Ke, Y. Liao, et al., "Rational Modeling and Design of Piezoelectric Biomolecular Thin Films Toward Enhanced Energy Harvesting and Sensing," *Advanced Functional Materials* 34 (2024): 2410566, https://doi.org/10.1002/adfm.202410566.

4. F. Yang, J. Li, Y. Long, et al., "Wafer-Scale Heterostructured Piezoelectric Bio-Organic Thin Films," *Science* 373 (2021): 337–342, https://doi.org/10.1126/science.abf2155.

5. Q. Wang, D. Hu, X. Huang, et al., "Hybrid Triboelectric-Electromagnetic-Electric Field Energy Harvester for Simultaneous Wind and Electric Field Energy Capture in High-Voltage Transmission System," *Advanced Energy Materials* 15 (2025): 2403931, https://doi.org/10.1002/aenm.202403931.

6. M. Zhou, S. Mao, Z. Wu, et al., "A Flexible Omnidirectional Rotating Magnetic Array for MRI-Safe Transdermal Wireless Energy Harvesting through Flexible Electronics," *Science Advances* 9 (2023): adi5451, https://doi.org/10.1126/sciadv.adi5451.

7. Z. Abdin, M. A. Alim, R. Saidur, et al., "Solar Energy Harvesting with the Application of Nanotechnology," *Renewable and Sustainable Energy Reviews* 26 (2013): 837–852, https://doi.org/10.1016/j.rser.2013.06.023.

8. J. Park, K. Kim, Y. Kim, et al., "A Wireless, Solar-Powered, Optoelectronic System for Spatial Restriction-Free Long-Term Optogenetic Neuromodulations," *Science Advances* 9 (2023): adi8918, https://doi.org/10.1126/sciadv.adi8918.

9. L. Long, W. Liu, Z. Wang, et al., "High Performance Floating Self-Excited Sliding Triboelectric Nanogenerator for Micro Mechanical Energy Harvesting," *Nature Communications* 12 (2021): 4689, https://doi.org/10.1038/s41467-021-25047-y.

10. L. Dong, G. Hu, Q. Tang, C. Zhao, F. Yang, and Y. Yang, "Advanced Aerodynamics-Driven Energy Harvesting Leveraging Galloping-Flutter Synergy," *Advanced Functional Materials* 35 (2025): 2414324.

11. Q. Yan and M. G. Kanatzidis, "High-Performance Thermoelectrics and Challenges for Practical Devices," *Nature Materials* 21 (2022): 503–513, https://doi.org/10.1038/s41563-021-01109-w.

12. K. Nan, S. D. Kang, K. Li, et al., "Compliant and Stretchable Thermoelectric Coils for Energy Harvesting in Miniature Flexible Devices," *Science Advances* 4 (2018): aau5849.

13. S. Pattipaka, J. Jeong, H. Choi, J. Ryu, and G.-T. Hwang, "Magneto-Mechano-Electric (MME) Composite Devices for Energy Harvesting and Magnetic Field Sensing Applications," *Sensors* 22 (2022): 5723.

14. V. Annapureddy, H. Palneedi, G.-T. Hwang, et al., "Magnetic Energy Harvesting with Magnetoelectrics: An Emerging Technology for Self-Powered Autonomous systems," *Sustainable Energy & Fuels* 1 (2017): 2039–2052, https://doi.org/10.1039/C7SE00403F.

15. J. Ryu, J.-E. Kang, Y. Zhou, et al., "Ubiquitous Magneto-Mechano-Electric Generator," *Energy & Environmental Science* 8 (2015): 2402–2408, https://doi.org/10.1039/C5EE00414D.

16. M. G. Kang, R. Sriramdas, H. Lee, et al., "High Power Magnetic Field Energy Harvesting through Amplified Magneto-Mechanical Vibration," *Advanced Energy Materials* 8 (2018): 1703313.

17. S. H. Kim, A. Thakre, D. R. Patil, et al., "Enhancement of Energy-Harvesting Performance of Magneto–Mechano–Electric Generators Through Optimization of the Interfacial Layer," *ACS Applied Materials & Interfaces* 13 (2021): 19983–19991, https://doi.org/10.1021/acsami.1c00922.

18. G. Liu, P. Ci, and S. Dong, "Energy Harvesting from Ambient Low-Frequency Magnetic Field Using Magneto-Mechano-Electric Composite Cantilever," *Applied Physics Letters* 104 (2014): 032908, https://doi.org/10.1063/1.4862876.

19. V. Annapureddy, M. Kim, H. Palneedi, et al., "Low-Loss Piezoelectric Single-Crystal Fibers for Enhanced Magnetic Energy Harvesting With Magnetoelectric Composite," *Advanced Energy Materials* 6 (2016): 1601244, https://doi.org/10.1002/aenm.201601244.

20. R. Sriramdas, M.-G. Kang, M. Meng, et al., "Large Power Amplification in Magneto-Mechano-Electric Harvesters Through Distributed Forcing," *Advanced Energy Materials* 10 (2020): 1903689, https://doi.org/10.1002/aenm.201903689.

21. J. Gao, D. Hasanyan, Y. Shen, Y. Wang, J. Li, and D. Viehland, "Giant Resonant Magnetoelectric Effect in Bi-Layered Metglas/Pb(Zr,Ti)O3 Composites," *Journal of Applied Physics* 112 (2012): 104101, https://doi.org/10.1063/1.4765724.

22. Z. Yu, J. Yang, J. Cao, et al., "A PMNN-PZT Piezoceramic Based Magneto-Mechano-Electric Coupled Energy Harvester," *Advanced Functional Materials* 32 (2022): 2111140, https://doi.org/10.1002/adfm.202111140.

23. K.-W. Lim, M. Peddigari, C. H. Park, et al., "A High Output Magneto-Mechano-Triboelectric Generator Enabled by Accelerated Water-Soluble Nano-Bullets for Powering a Wireless Indoor Positioning System," *Energy & Environmental Science* 12 (2019): 666–674, https://doi.org/10.1039/C8EE03008A.

24. H. Song, D. R. Patil, W.-H. Yoon, et al., "Significant Power Enhancement of Magneto-Mechano-Electric Generators by Magnetic Flux Concentration," *Energy & Environmental Science* 13 (2020): 4238–4248, https://doi.org/10.1039/D0EE01574A.

25. D. R. Patil, S. Lee, S. H. Park, J. Ryu, and D.-Y. Jeong, "Boosting the Performance of Magneto-Mechano-Electric Energy Generator Using Magnetic Lens," *Sensors and Actuators A: Physical* 338 (2022): 113451, https://doi.org/10.1016/j.sna.2022.113451.

26. H. Lee, R. Sriramdas, P. Kumar, M. Sanghadasa, M. G. Kang, and S. Priya, "Maximizing Power Generation from Ambient Stray Magnetic Fields around Smart Infrastructures Enabling Self-Powered Wireless

Devices," *Energy & Environmental Science* 13 (2020): 1462–1472, https://doi.org/10.1039/C9EE03902C.

27. Z. Yu, J. Yang, L. Xu, et al., "Giant Tridimensional Power Responses in a T-Shaped Magneto–Mechano–Electric Energy Harvester," *Energy & Environmental Science* 17 (2024): 1426–1435, https://doi.org/10.1039/D3EE03634K.

28. Y. Yu, Z. Cheng, J. Chang, et al., "Enhanced In-Plane Omnidirectional Energy Harvesting From Extremely Weak Magnetic Fields via Four-fold Symmetric Magneto-Mechano-Electric Coupling," *Advanced Energy Materials* 14 (2024): 2402487, https://doi.org/10.1002/aenm.202402487.

29. X. Zheng, Z. Cheng, B. Wang, et al., "A Self-Powered Double U-Finger MME Resonator Capable of Wirelessly Capturing Abnormal Message in Smart Grid Networks," *Advanced Science* 12 (2025): 08149.

30. Z. Yu, H. Qiu, Z. Chu, et al., "Significant Output Power Enhancement in Symmetric Dual-Mode Magneto-Mechano-Electric Coupled Resonators," *Advanced Energy Materials* 12 (2022): 2202306.

31. S. Dong, J. Zhai, J. F. Li, D. Viehland, and S. Priya, "Multimodal System for Harvesting Magnetic and Mechanical Energy," *Applied Physics Letters* 93 (2008): 103511, https://doi.org/10.1063/1.2982099.

32. Y. Zhou, D. J. Apo, and S. Priya, "Dual-Phase Self-Biased Magnetoelectric Energy Harvester," *Applied Physics Letters* 103 (2013): 192909, https://doi.org/10.1063/1.4829151.

33. H.-C. Song, P. Kumar, R. Sriramdas, et al., "Broadband Dual Phase Energy Harvester: Vibration and Magnetic Field," *Applied Energy* 225 (2018): 1132–1142, https://doi.org/10.1016/j.apenergy.2018.04.054.

34. D. R. M. Milne, L. M. Le Pen, D. J. Thompson, and W. Powrie, "Properties of Train Load Frequencies and their Applications," *Journal of Sound and Vibration* 397 (2017): 123–140, https://doi.org/10.1016/j.jsv.2017.03.006.

35. S. Yang, L. Chouinard, S. Langlois, P. Van Dyke, and J. Paradis, "Predicting Distribution of Aeolian Vibration Amplitude of Undamped Overhead Transmission Lines," *Journal of Wind Engineering and Industrial Aerodynamics* 250 (2024): 105779, https://doi.org/10.1016/j.jweia.2024.105779.

36. J. Zuo, L. Dong, F. Yang, Z. Guo, T. Wang, and L. Zuo, "Energy Harvesting Solutions for Railway Transportation: A Comprehensive Review," *Renewable Energy* 202 (2023): 56–87.

37. G. Guastadisegni, S. De Pinto, D. Cancelli, et al., "Ride analysis tools for passenger cars: Objective and subjective evaluation techniques and correlation processes—a review," *Vehicle System Dynamics* 62 (2024): 1876–1902.

38. Z. Chu, Z. Sun, B. Wang, et al., "Significantly Enhanced Power Generation from Extremely Low-Intensity Magnetic Field via a Clamped-Clamped Magneto-Mechano-Electric Generator," *Advanced Energy Materials* 12 (2022): 2103345.

39. X. He, Y. Xu, J. Wu, et al., "Enhanced Power Density by Resonant Frequency Optimization in Magneto-Mechano-Electric Generator for Multifunctional Wireless Sensor System," *Small* 21 (2025): 2412214.

40. Y. Xu, X. He, X. Liang, et al., "Multiple-Coupling Optimization Strategy for Significantly Enhancing the Output Power Density of a Compact Magneto-Mechano-Electric Energy Harvester," *Energy & Environmental Science* 18 (2025): 8339–8351, https://doi.org/10.1039/D5EE01346A.

41. J. Chang, X. Gao, W. Peng, et al., "A Dragonfly-Wing-Like Energy Harvester with Enhanced Magneto-Mechano-Electric Coupling," *Device* 1 (2023): 100021, https://doi.org/10.1016/j.device.2023.100021.

42. R. Sriramdas, D. Yang, M.-G. Kang, M. Sanghadasa, and S. Priya, "Universal Multienergy Harvester Architecture," *ACS Applied Materials & Interfaces* 13 (2021): 324–331, https://doi.org/10.1021/acsami.0c15075.

43. A. Kumar, S. H. Park, D. R. Patil, G.-T. Hwang, and J. Ryu, "Effect of Aspect Ratio of Piezoelectric Constituents on the Energy Harvesting Performance of Magneto-Mechano-Electric Generators," *Energy* 239 (2022): 122078.

44. Y. Kuang, Z. J. Chew, T. Ruan, et al., "Magnetic Field Energy Harvesting from the Traction Return Current in Rail Tracks," *Applied Energy* 292 (2021): 116911, https://doi.org/10.1016/j.apenergy.2021.116911.

45. W. Zhai, K. Wang, and C. Cai, "Fundamentals of Vehicle–Track Coupled Dynamics," *Vehicle System Dynamics* 47 (2009): 1349–1376.

Supporting Information

Additional supporting information can be found online in the Supporting Information section.

Supporting File: aenm70683-sup-0001-SuppMat.docx.

Supplementary Movie S1: aenm70683-sup-0002-Movie S1.mp4.

Supplementary Movie S2: aenm70683-sup-0004-Movie S2.mp4.

Supplementary Movie S3: aenm70683-sup-0004-Movie S3.mp4.